

## The Western Australia Modeling project — Part 2: Seismic validation

Jeffrey Shragge<sup>1</sup>, David Lumley<sup>2</sup>, Julien Bourget<sup>3</sup>, Toby Potter<sup>4</sup>, Taka Miyoshi<sup>5</sup>, Ben Witten<sup>6</sup>, Jeremie Giraud<sup>7</sup>, Thomas Wilson<sup>8</sup>, Afzal Iqbal<sup>9</sup>, Mohammad Emami Niri<sup>10</sup>, and Beau Whitney<sup>11</sup>

### Abstract

Large-scale 3D modeling of realistic earth models is being increasingly undertaken in industry and academia. These models have proven useful for various activities such as geologic scenario testing through seismic finite-difference (FD) modeling, investigating new acquisition geometries, and validating novel seismic imaging, inversion, and interpretation methods. We have evaluated the results of the Western Australia (WA) Modeling (WAMo) project, involving the development of a large-scale 3D geomodel representative of geology of the Carnarvon Basin, located offshore of WA's North West Shelf (NWS). Constrained by a variety of geologic, petrophysical, and field seismic data sets, the viscoelastic WAMo 3D geomodel was used in seismic FD modeling and imaging tests to "validate" model realizations. Calibrating the near-surface model proved to be challenging due to the limited amount of well data available for the top 500 m below the mudline. We addressed this issue by incorporating additional information (e.g., geotechnical data, analog studies) as well as by using soft constraints to match the overall character of nearby NWS seismic data with the modeled shot gathers. This process required undertaking several "linear" iterations to apply near-surface model conditioning, as well as "nonlinear" iterations to update the underlying petrophysical relationships. Overall, the resulting final WAMo 3D geomodel and accompanying modeled shot gathers and imaging results are able to reproduce the complex full-wavefield character of NWS marine seismic data. Thus, the WAMo model is well-calibrated for use in geologic and geophysical scenario testing to address common NWS seismic imaging, inversion, and interpretation challenges.

### Introduction

Developing a high-resolution 3D geomodel that represents the state of geologic and geophysical knowledge at a particular earth location is an important process for hydrocarbon exploration and reservoir development. Geomodels can be developed at a variety of model sizes (i.e., from reservoir to basin) and resolution length scales, have differing levels of realism based on the physical constraints used in the geomodeling process, and can be used for a wide variety of purposes (e.g., geologic-, reservoir-, or flow-scenario testing; seismic acquisition and illumination analysis; and benchmark-

ing new seismic imaging, inversion, and interpretation methods). Numerous examples of 2D and 3D geomodels exist in the public domain, including modeling of specific geologic scenarios of offshore West Africa (Versteeg, 1994), the Canadian Foothills (Gray and Marfurt, 1995; Regone et al., 2017), the Gulf of Mexico (Billette and Brandsberg-Dahl, 2005), conventional oil traps (Lee and Mukerji, 2012), as well as recent SEG Advanced Modeling (SEAM) work on the North American unconventional and Arabian Desert Arid environments (Regone et al., 2017). These geomodels span a wide range of geologic and geophysical complexity,

<sup>1</sup>Colorado School of Mines, Center for Wave Phenomena, Geophysics Department, Golden, Colorado, USA. E-mail: jshragge@gmail.com (corresponding author).

<sup>2</sup>University of Texas at Dallas, School of Natural Sciences and Mathematics, Dallas, Texas, USA and University of Western Australia, School of Physics, Mathematics and Computing, Perth, Australia. E-mail: david.lumley@utdallas.edu.

<sup>3</sup>Total SA, Pau, France. E-mail: julien.bourget@uwa.edu.au.

<sup>4</sup>Pelagos Consulting and Education, Perth, Australia. E-mail: toby@pelagos-consulting.com.

<sup>5</sup>Research Institute of Innovative Technology for the Earth, Tokyo, Japan. E-mail: taka.miyoshi@gmail.com.

<sup>6</sup>Nanometrics Inc., Ottawa, Ontario, Canada. E-mail: bwitten@gmail.com.

<sup>7</sup>The University of Western Australia, Centre for Exploration Targeting, School of Earth Sciences, Crawley, Australia. E-mail: jeremie.giraud@research.uwa.edu.au.

<sup>8</sup>Eliis Paleoscan, Perth, Australia. E-mail: tctwilson@gmail.com.

<sup>9</sup>The University of Western Australia, School of Earth Sciences, Crawley, Australia. E-mail: afzal.iqbal@uwa.edu.au.

<sup>10</sup>University of Tehran, Institute of Petroleum Engineering, College of Engineering, Tehran, Iran. E-mail: mohammad1199@gmail.com.

<sup>11</sup>Geoter SAS-Fugro Group, Castries 34160, France. E-mail: bbwhitney@gmail.com.

Manuscript received by the Editor 23 November 2018; revised manuscript received 2 April 2019; published ahead of production 16 July 2019; published online 20 September 2019. This paper appears in *Interpretation*, Vol. 7, No. 4 (November 2019); p. T793–T807, 15 FIGS., 2 TABLES. <http://dx.doi.org/10.1190/INT-2018-0218.1>. © 2019 Society of Exploration Geophysicists and American Association of Petroleum Geologists. All rights reserved.

from basic structural models with smooth layer properties, to highly complex heterogeneous stratigraphic models constrained by field geologic, petrophysical, and seismic data.

During the earlier stages of hydrocarbon exploration and field development, the state of knowledge usually consists of a limited number of boreholes, a broad understanding of the structural and stratigraphic geology environment, and a variety of 2D/3D seismic data. In this context, a typical goal would be to use the available information to develop a realistic 3D geomodel that can be used to test 3D seismic imaging/inversion results, simulate different reservoir scenarios, and other objectives. Borehole data are used to provide high-resolution (i.e., often cm scale) 1D constraints on the vertical P- and S-wave velocity ( $V_P$  and  $V_S$ ), density ( $\rho$ ), and lithology of units intersected by the well; however, because borehole measurements are geographically restricted due to a limited number of well locations and depths, this information needs to be upscaled and laterally interpolated/extrapolated to create a 3D geologic model and to match the expected response within the frequency band of 3D seismic data. Conversely, although 3D seismic observations can be used to develop realistic 3D geologic structure and seismic stratigraphy (i.e., chronostratigraphic surfaces, facies, and layering) throughout a geomodel, the relatively low vertical resolution (10s of meters) of 3D seismic data (i.e., relative to borehole information, geologic variation, and common model sampling intervals) largely precludes constraining finer scale 3D petrophysical variations that can greatly affect the observed seismic waveform responses.

Closing the gap in length scales between 1D borehole and 3D seismic observations in geomodeling activities requires introducing additional information, usually through statistical rock-physics relationships. Although empirical relationships can be used in this context, a more robust approach would be to develop a probabilistic petrophysical model conditioned by local borehole observations down to the seismic facies level. The resulting petrophysical distributions then allow users to draw representative samples and fully populate each geomodel unit with elastic ( $V_P$ ,  $V_S$ , and  $\rho$ ) material property values (Doyen, 2007). Ideally, the resulting 3D geomodel realization would (1) represent realistic material property values at each model location, (2) provide a realistic spatial distribution of trends observable at the level of geologic layers, facies, or sequences, (3) honor the borehole/seismic data used to develop or constrain the model, and (4) not violate any known geologic principles (e.g., stratigraphy, age relationships, and topology) or geophysical relationships (e.g., physically realizable  $V_P/V_S$  ratio, positive bulk and shear moduli,  $K$  and  $G$ ). By following such an approach, one may generate a geologically and petrophysically realistic geomodel.

It is increasingly being recognized, though, that this strategy does not provide sufficient validation of 3D

geomodels. In particular, this approach in no way guarantees that such a geomodel will result in realistic seismic data when attempting to “close the loop” by comparing field data with 2D/3D seismic forward-modeling results. Moreover, even approximating full-wavefield behavior with 1D convolutional seismic modeling (i.e., convolving a wavelet with the calculated geomodel reflectivity) is insufficient for predicting amplitude versus angle behavior at farther source-receiver offsets in which  $V_S$  and  $\rho$  increasingly control reflection amplitude behavior or for understanding multiple scattering effects. Thus, it is important to invest in full-wavefield viscoelastic modeling to more accurately simulate such significant seismic processing, imaging, inversion, and interpretation challenges as (1) short-period multiples, (2) wave-propagation effects of complex near-surface short-wavelength structure (i.e., carbonate reefs and canyons), (3) scattering from strong overburden heterogeneity, and (4) realistic refracted arrivals important for successful full-waveform inversion applications.

In this paper, we investigate the importance of full-wavefield viscoelastic seismic modeling and acoustic reverse time migration (RTM) in fine tuning and “validating” 3D geomodels developed by the geologic/petrophysical geomodeling approach (Shragge et al., 2019, Part 1). We conduct these investigations in the context of a large-scale ( $80 \times 40 \times 6 \text{ km}^3$ ) 3D geomodel of a block of the Northern Carnarvon Basin (NCB) located on Western Australia’s (WA’s) North West Shelf (NWS). As the focus of the joint industry-academia Western Australian Modeling (WAMo) project, we constructed this 3D geomodel using geologic and petrophysical constraints from 22 regional wells and a 3D seismic “mega-merge” volume covering nearly the entire model area.

One key WAMo project design decision was to not construct a model that exactly reproduced field seismic data of a specific NCB block; rather, it was to develop a realistic 3D geomodel that broadly honored the geologic and petrophysical observations while replicating the overall “character” of NCB 3D field seismic data. Over a three year period, we developed several WAMo overburden model variations that allowed us to explore a wide range of full-wavefield viscoelastic behavior. Overall, this iterative validation methodology proved to be an essential component in the context of developing a calibrated 3D WAMo geomodel capable of reproducing realistic synthetic 2D/3D seismic data sets that accurately represent the significant NCB and NWS seismic imaging, inversion, and interpretation challenges.

We begin by reviewing our 3D geomodeling approach and highlighting the WAMo geomodel features important in the context of this study. Readers interested in a detailed explanation of the geomodel building process, parameterization, and quality control are referred to the Part 1 paper (Shragge et al., 2019). We then describe our viscoelastic seismic modeling activities, as well as our choices in acquisition design, modeling parameters, and the WAMo source wavelets used to simulate the 2D and 3D seismic data sets. Subsequently,

we present seismic shot-gather modeling and RTM results using the final WAMo model, and we compare these to representative examples of NCB field data. We discuss the importance of fine-tuning 3D geomodels by presenting modeling results for three iterations of WAMo model realizations that illustrate the wide range of seismic character exhibited when modifying near-surface overburden model components. The paper concludes with a summary of the main findings and insights from the WAMo project that may be important for other geoscientists considering a similar 3D geomodeling and validation exercise.

### WAMo geomodel overview

The 3D WAMo geomodel represents an  $80 \times 40 \times 6 \text{ km}^3$  block of the NCB that incorporates the shallow continental shelf, shelf break, and deepwater geologic environments. The WAMo model was constrained using data from 22 nearby wells and a 3D seismic mega-merge volume representing an amalgamation of 12 regional processed and phase-matched 3D seismic prestack time migration (PSTM) image volumes. This section summarizes the geologic and petrophysical modeling procedures used to develop the WAMo geomodel. For a more complete narrative, the reader is referred to [Shragge et al. \(2019\)](#).

### Chronostratigraphic modeling

We extracted 13 main chronostratigraphic surfaces from the 3D seismic mega-merge volume (see Figure 1) covering the  $80 \times 40 \text{ km}^2$  WAMo model area, except for sections located in the deep water where only regional 2D seismic lines were available as constraints. These surfaces, extracted on a regular  $25 \times 25 \text{ m}^2$  grid, were

smoothed and edited based on seismic stratigraphic principles and subsequently converted from time to depth using a regional 3D migration velocity model. Individual mesh frameworks were constructed for each of the 12 resulting stratigraphic units. Each stratigraphic unit was modeled individually using a zonation procedure that distributed several different seismic sequences as constrained by available core samples, well-log reports, biostratigraphy, and 3D seismic interpretation. Layering, representing the finest geologic unit, was introduced within each zone. The various sequences and layers were then populated with representative lithology based on the information obtained from examining available cuttings and sidewall cores, core logs, and completion report data. We determined the dominant sedimentary facies at the sequence level, and we created an index volume for cross-referencing during the subsequent petrophysical modeling activities (see the description chart in the lower left of Figure 1).

### Geobody modeling

Introducing geobodies associated with shorter-wavelength geological features [e.g., (paleo)canyons, carbonate reefs, cemented aeoleanite bodies] required additional model building efforts. In most instances, representative geobodies could be auto-picked directly from the 3D seismic mega-merge volume based on a combination of geometric or amplitude attributes. Extracted features were imported into the WAMo geomodel in a modular fashion (i.e., they could be “turned on or off” depending on the particular geomodeling goals). Special attention was placed on realistic modeling of problematic dolomitic intervals (e.g., the Bare formation [Fm]), carbonate reefs, ooids, canyon fill and mass

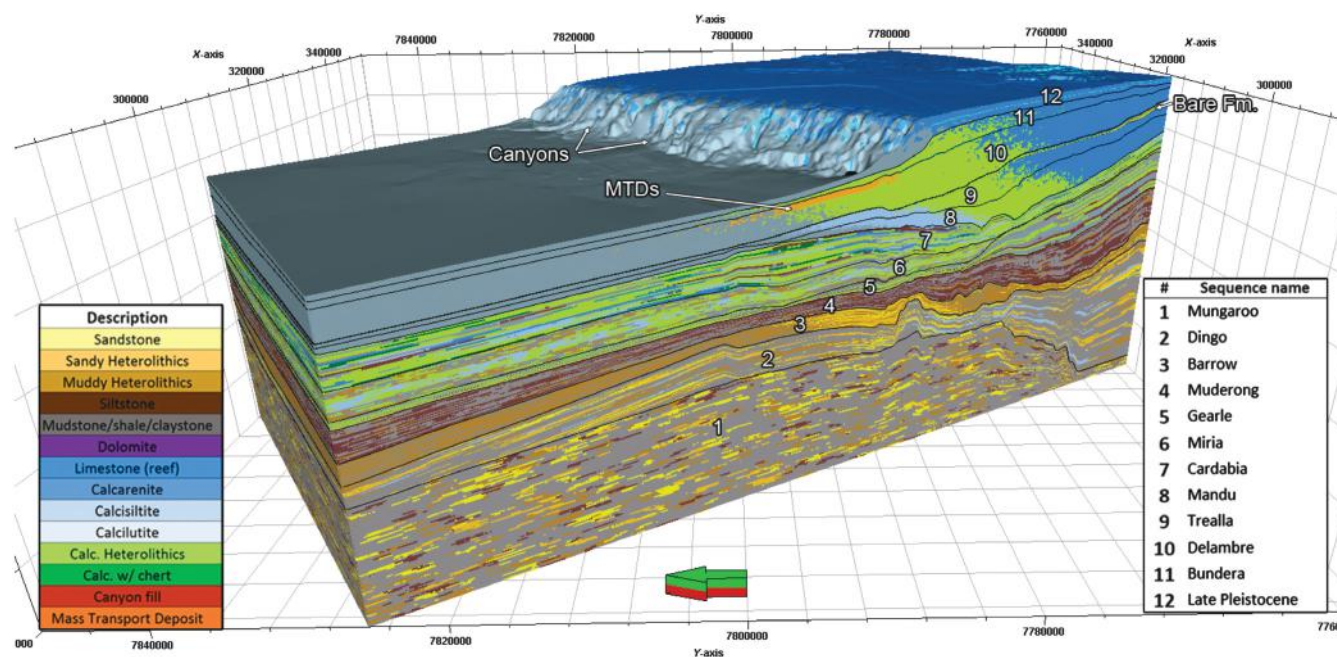


**Figure 1.** Visualization of the 3D WAMo geomodel showing the 12 stratigraphic sequences color coded by the different seismic facies. Also evident are the present-day canyons, mass transport deposits (MTDs), and the Bare Fm.



transport deposits, all of which pose significant NCB imaging, inversion and interpretation challenges.

### Petrophysical modeling

We performed petrophysical modeling to populate each of the seismic facies described above. Processed and despiked log data from 18 of 22 available wells were of sufficient quality for compiling geostatistical histograms for each WAMo model stratigraphic sequence. We estimated vertical and horizontal variograms for use in lithofacies modeling, based on log-data analysis and seismic interpretation, respectively, and we subsequently generated 3D geostatistical realizations unit by unit for the three elastic parameter fields ( $V_P$ ,  $V_S$ , and  $\rho$ ) using the variograms to guide the spatial distribution of each facies. The resulting geomodel realizations were tested for physical realizability based on  $V_P/V_S$  ratio as well as for positivity of calculated bulk and shear moduli ( $K$  and  $G$ , respectively). Finally, up-scaled petrophysical models output unit by unit at a spatial sampling of  $[\Delta x, \Delta y, \Delta z] = [25, 25, 5]$  m were combined into a global WAMo elastic model in SEG-Y format for use in 2D/3D viscoelastic FD modeling activities.

### 3D viscoelastic modeling

Modeling 2D/3D synthetic seismic data with a realism broadly consistent of field observations requires using a high-order approximation of wave-propagation physics. Based on discussions involving all of the project participants, we concluded that an isotropic viscoelastic parameterization was necessary and sufficient to model seismic data of a sufficient level of accuracy to adequately exhibit the types of imaging, inversion, and interpretation challenges discussed by [Shragge et al. \(2019\)](#). Relative to viscoacoustic seismic modeling algorithms, viscoelastic implementations simulate more realistic amplitude variation with offset behavior, attenuation losses, and full-wavefield behavior (e.g., P-S wave conversions at strong-contrast interfaces) ([Aki and Richards, 1980](#)).

We performed our 2D and 3D viscoelastic seismic modeling activities using in-house optimized versions of the open-source SOFI2D and SOFI3D seismic modeling codes ([Bohlen, 2002](#)). The SOFI codes use a velocity-stress formulation to solve the isotropic viscoelastic wave equation using FD operators with either Taylor-series or optimized Holberg coefficients applied on a staggered grid. The numerical accuracy of FD approximations can be specified from  $O(\Delta x^2, \Delta t^2)$  to  $O(\Delta x^{12}, \Delta t^4)$ ; however, based on our preferred trade-off between computational runtime and numerical accuracy, we selected optimized Holberg coefficients of eighth-order accuracy in space and second-order accuracy in time (i.e.,  $O(\Delta x^8, \Delta t^2)$ ) for all of the modeling results reported below.

The SOFI codes require input  $[V_P, V_S, \rho, Q_P, Q_S]$  models, the source wavelet, as well as the source injection point and receiver locations. For the attenuation mod-

els, we selected effective values of  $Q_P = Q_S = 135$  within nonwater model components based on the NCB field data experience of our industry partners. Achieving these effective  $Q$  values required specifying  $Q_P = Q_S = 120$  within the SOFI codes, assuming a single relaxation mechanism and a 48 Hz reference frequency. Within the water layer, we used large  $Q_P = Q_S = 1000$  values to reduce attenuation to negligible levels. We constructed the  $Q_P$  and  $Q_S$  fields directly from the  $V_S$  model by setting  $Q_P = Q_S = 1000$  wherever  $V_S = 0.0$  km/s and  $Q_P = Q_S = 120$  otherwise.

Complex perfectly matched layer (C-PML) boundary conditions were used to prevent reflections back into the interior from waves interacting with the computational domain boundary. We completed a parameter testing investigation to optimize the C-PML response. Based on these tests, we applied a 40-point C-PML boundary layer for 2D and 3D modeling runs. Finally, we optimized the Message Passing Interface (MPI) parallelization of the SOFI codes for use on the Pawsey Center Magnus cluster high-performance computing (HPC) environment. As part of the WAMo project work, the SOFI3D code went through extensive optimization and MPI tuning, as well as through strong and weak scaling tests for different submodel volumes and 3D domain-decomposition geometries, respectively. These scaling results were tabulated and used to guide MPI parameter selection for our 2D/3D viscoelastic modeling activities.

### Acquisition design

Due to limitations on the total available computing resource, several key decisions were made regarding computational trade-offs in the WAMo seismic modeling acquisition design (e.g., grid size and sampling, maximum frequency content, and minimum model velocity; see, e.g., [Fehler and Keliher, 2011](#)). One of the key project design goals was to model 2D/3D seismic data with realistic frequency content. Based on this criterion, we set target cutoff frequencies of 75 and 55 Hz for 2D and 3D viscoelastic modeling, respectively. Simulating largely dispersion-free seismic data up to these target frequencies required uniform grid spacing of 3.125 and 5.0 m for 2D and 3D modeling runs, respectively. Because the output WAMo elastic model parameter grids were constructed at a larger spatial sampling, we interpolated all parameter fields using splines under tension (vertically) and distance-based averaging (laterally) to create a uniformly sampled 5.0 m 3D mesh. We note that the product  $f_{\max} \times dx$  (here 55 Hz  $\times$  5 m) is similar to that used in the SEAM I project: 30 Hz  $\times$  10 m ([Fehler and Keliher, 2011](#)). We generated regularly sampled 2D models by first extracting the desired 2D plane at the coarser sampling and then applying 2D distance-based averaging to obtain the equivalent model at the desired uniform 3.125 m sampling interval.

Another key modeling decision was whether to threshold the  $V_S$  field. Based on the initial modeling

tests, we determined that setting a minimum (nonzero)  $V_S = 0.7$  km/s represented a necessary trade-off among computational run time, numerical accuracy, and data realism. Although the subsequent filtering activities effectively restricted the range of water-bottom behavior that could be modeled to medium or strong “hardness,” this trade-off was deemed acceptable for the realized improvements in simulated data quality and quantity permitted by our total available computational resources. We implemented this threshold by first applying a cutoff filter to the entire  $V_S$  model, and then altering the  $V_P$  model to ensure a physically realizable  $V_P/V_S$  ratio.

### Model parameters

Table 1 presents the parameters used for 2D and 3D viscoelastic FD modeling. For 3D modeling, the computational domains were set at  $[N_x, N_y, N_z] = [2200, 800, 1200]$  grid points representing an aperture of  $[11.0, 4.0, 6.0]$  km in the inline, crossline, and depth dimensions at the uniform 5.0 m grid spacing. To satisfy the Courant-Fredericks-Levy (CFL) condition (Courant et al., 1928) for 3D modeling, we set the time sampling interval to  $dt = 0.375$  ms. For spectral information, see the WAMo wavelet discussion below. We determined the maximum simulation time  $t_{\max} = 6.0$  s based on the two-way traveltime (TWT) from the base of the model to the farthest modeled source-receiver offset. The 2D FD modeling runs used simulation grids of  $[N_x, N_z] = [3520, 1920]$  at a uniform 3.125 m spacing leading to modeling apertures of  $[11.0, 6.0]$  km in the inline and depth directions, respectively. The time sample interval and maximum simulation time for 2D modeling work were set at  $dt = 0.2$  ms and  $t_{\max} = 6.0$  s, with the former reduced from the 3D modeling  $dt$  value to satisfy CFL stability requirements for the finer 2D computational mesh.

Table 2 summarizes the key parameters used for 2D/3D seismic modeling. The first five entries show the source parameters, such as the wavelet and transient frequency as well as the shot depth, interval, and type. The remaining 10 entries detail the receiver or streamer acquisition parameters. The 3D viscoelastic modeling runs involved injecting a source wavelet at 5 m depth and outputting simulated data at a spatial sampling of  $dr_x = dr_y = 10.0$  m to a maximum of 8.0 km of inline and  $\pm 1.8$  km of crossline offset, respectively. The 2D modeling runs involved injecting a seismic source at 6.25 m depth and

outputting single-streamer data at  $dr_x = 9.375$  m to a maximum of 8.0 km inline offset. The 2D (3D) shot-gather modeling required extracting the pressure response from the 2D (3D) viscoelastic wavefields at intervals of  $dt = 2.0$  ms ( $dt = 3.0$  ms).

### WAMo wavelet

One project design goal was to generate a 3D “WAMo wavelet” having a largely flat far-field spectrum (i.e., after propagating 10 wavelengths) between 4 and 50 Hz after taking the free-surface ghost contribution into consideration. We achieved this by first defining a function with a flat frequency spectrum that when tapered allowed for a smooth user-defined roll off at 4 and 50 Hz. We then created a second “ghost version” of this wavelet with the appropriate phase lag for the 5 m source depth. After deconvolving the ghost wavelet from the original wavelet (effectively boosting the lower frequency components), we applied Kolmogoroff spectral factorization (Claerbout, 1998) to generate the

**Table 1. FD modeling parameters used for the 2D and 3D viscoelastic modeling runs.**

Parameter (unit)	2D	3D
Grid points (depth $\times$ inline $\times$ crossline)	1920 $\times$ 3520	1200 $\times$ 2200 $\times$ 800
Grid intervals (m)	3.125	5.000
FD time interval (ms)	0.200	0.375
Simulation time (s)	6.0	6.0
Number of time steps	30,001	16,001
PML boundary size (grid points)	40	40

**Table 2. Source and acquisition parameters used for 2D and 3D FD modeling.**

Parameter (unit)	2D	3D
Source wavelet	2D WAMo wavelet	3D WAMo wavelet
Transient frequency (Hz)	75	55
Shot depth (m)	6.25	5
Shot intervals (m)	25	25
Source type	Explosive	Explosive
Number of receivers per streamer	1280	800
Receiver (group) spacing (m)	6.25	10
Minimum offset (m)	75	100
Number of streamers	1	360
Streamer separation intervals (m)	—	10
Streamer depth (m)	9.375	10
Record length (s)	6	6
Sampling interval (ms)	2	3
Samples per trace	3001	2001
Recording component	Pressure	Pressure

minimum-phase wavelet used for WAMo 3D modeling purposes. This wavelet “prefiltering” helped to reduce source-ghost notch filtering effects and generate a broadband response.

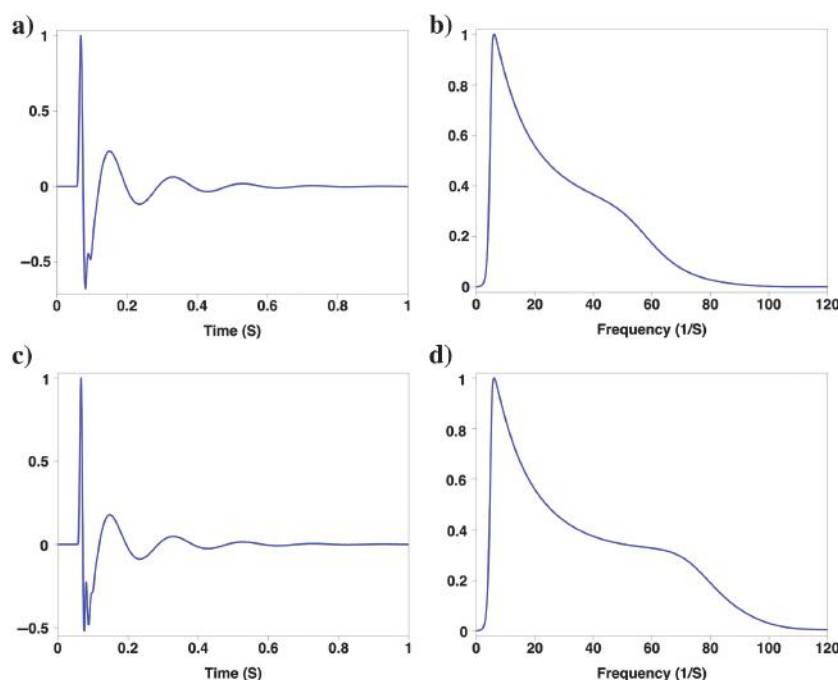


**Figure 2.** WAMo wavelet used for 2D and 3D FD modeling. (a) Time-domain 55 Hz 3D WAMo wavelet, (b) spectrum of 55 Hz 3D WAMo wavelet from (a), (c) time-domain 75 Hz 2D WAMo wavelet, and (d) spectrum of the 75 Hz 2D WAMo wavelet from (c).

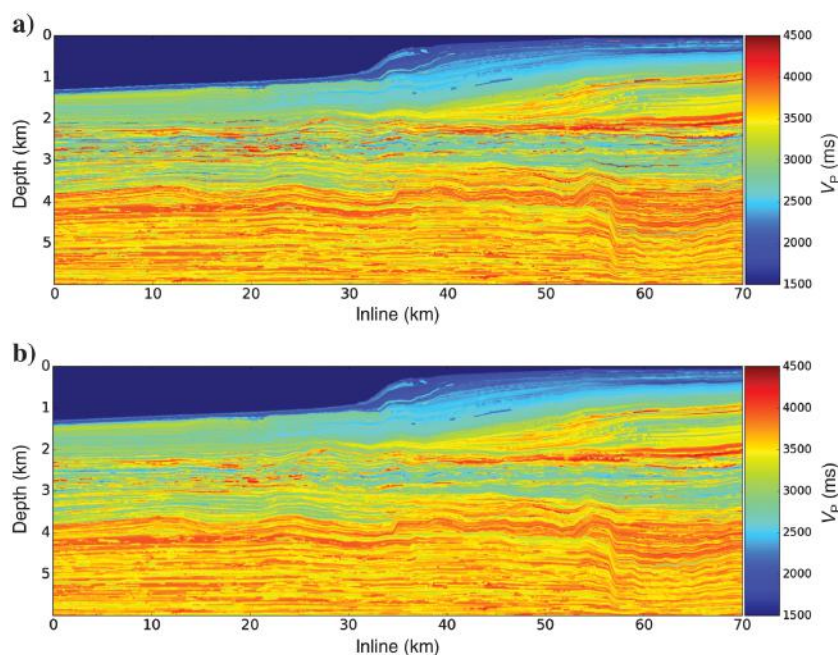


**Figure 3.** Example inline section extracted at 32 km crossline coordinate from the  $V_p$  component of the 3D WAMo geomodel. (a) Original  $V_p$  model interpolated to uniform 5 m sampling. (b) The  $V_p$  model from (a) after applying the two filtering operations to reduce scattering from staircasing and strong vertical short-wavelength heterogeneity.

Figure 2a–2d shows the 3D 55 Hz (2D 75 Hz) WAMo wavelet in the time and frequency domains, respectively. Although the time-domain WAMo wavelets appear initially quite impulsive with significant high-frequency content visible in the first 0.1 s, lower frequency oscillations dominate at later times (0.1–0.4 s). The 2D and 3D frequency spectra are similar in shape, with both exhibiting a large low-frequency boost between 3 and 15 Hz. However, the 3D WAMo wavelet spectrum falls off more quickly at higher frequencies to satisfy the stricter antidispersion requirements when performing 3D FD modeling on a coarser grid.

### Final model calibration

Initial FD modeling tests using the above parameters suggested that the short-wavelength structure of the earlier 3D WAMo geomodel iterations produced significant wavefield scattering judged to be too strong to be representative of NCB field data. Two main factors were found to contribute to these observations: Cartesian discretization of curvilinear model surfaces (i.e., staircasing) and overly strong short-wavelength vertical heterogeneity. To minimize staircasing, we applied a 2D or 3D triangle smoothing operator of 25 m width in all model dimensions (i.e., slowness to preserve traveltimes). To reduce the intensity of vertical model variability, we used the following near-surface model smoothing procedure: (1) Apply two passes of a 45 m 1D triangle filter to the (laterally smoothed) reciprocal model parameters  $\mathbf{m}_0$  in the vertical direction to create a smooth model  $\mathbf{m}_s$ , (2) calculate the short-wavelength components by subtracting  $\Delta\mathbf{m} = \mathbf{m}_s - \mathbf{m}_0$ , and (3) add back 50% of the defined short-wavelength structure model to generate a new model  $\mathbf{m}_n = \mathbf{m}_0 + \Delta\mathbf{m}/2$ . Figure 3a and 3b presents an extracted inline slice taken through the WAMo model at the 32 km crossline coordinate. Overall, the model appears laterally smoother and with less significant vertical velocity variation, which should be expected given the two model smoothing operations discussed above.

### Seismic modeling and imaging results

This section presents the viscoelastic modeling results using the filtered 3D viscoelastic model. The 2D modeling



efforts involving simulating a grid of 2D sail lines at a 25 m shot spacing at 5 km sail line intervals throughout the entire model. For the purpose of the current discussion, we focus on a single sail line located at the 32 km crossline coordinate that contains many of the important geomodel features of interest (i.e., shallow hard water bottom, Bear Fm, complex shelf break, deepwater section). A single 3D sail line of 50 km length with a shot aperture of 11 km and  $\pm 1.8$  km in the inline and crossline directions was also modeled along the selected crossline transect. However, for presentation purposes, we focus on 2D modeled data due to their more realistic frequency content and comparability to field seismic data observations.

### Near-offset section comparisons

Figure 4 compares 20 km long near-offset sections for the WAMo synthetic seismic modeling results and

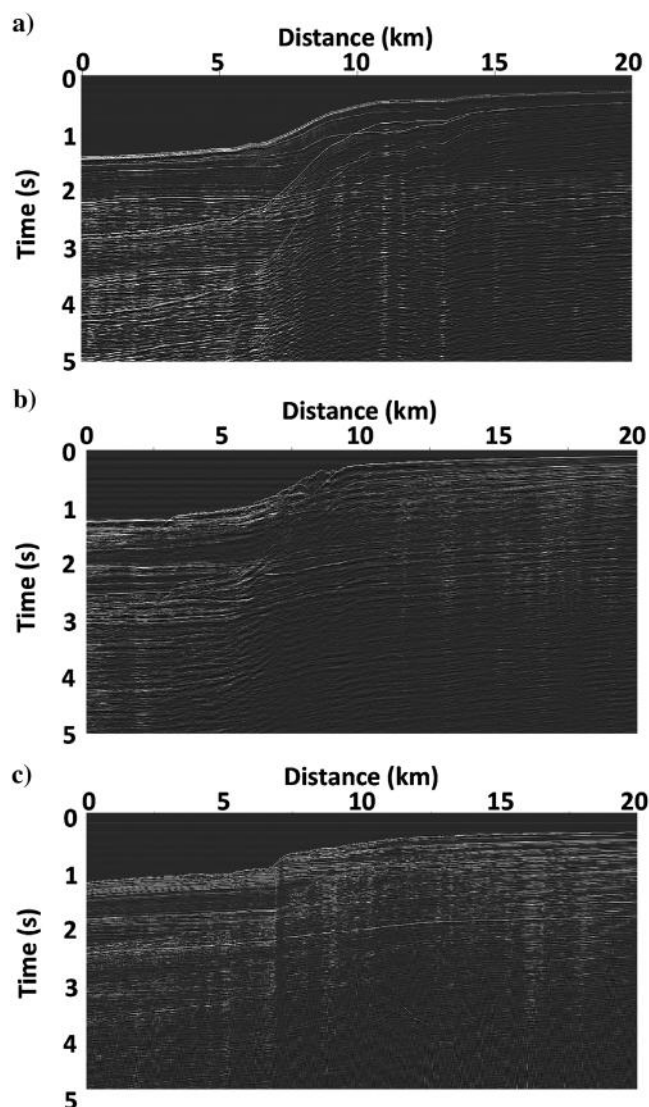


**Figure 4.** Near-offset section (75 m) for synthetic and field data sets. (a) The WAMo V3.2 model, (b) 3D Wheatstone broadband seismic data set within the WAMo area, and (c) conventional 3D NCB seismic data 25 km north of WAMo project area.

two representative NCB marine seismic data sets. Figure 4a presents a section modeled along the 2D line shown in Figure 3b extracted from the WAMo geomodel at the 32 km crossline coordinate. The deepwater sections clearly show strong reflection coefficients from the seabed and shallow layering. Also evident are the first-order and weak second-order free-surface multiples. Note that high-order short-period multiples in the shallow water make identifying the contributions from underlying primary reflections fairly difficult. Vertical amplitude streaking from near-surface focusing effects are also prominent at numerous locations in the image.

Figure 4b shows the near-offset section extracted from a single streamer cable of the Wheatstone 3D broadband marine data set acquired within the WAMo geomodel polygon. In comparison with Figure 4a, we note that the section shows a similar overall character including brightening of reflectivity in the deep water, the presence of first order but quite weak second-order free-surface multiples, vertical amplitude streaking, and complex short period multiples, though in significantly shallower water. Overall, the reflectivity on the shelf appears to be stronger than in the synthetic WAMo model results. Figure 4c presents a near-offset section from a conventional NCB 3D marine seismic survey acquired 25 km north of the WAMo project area in a region of gentler shelf break and somewhat deeper bathymetry. The overall character looks fairly similar, and it again includes vertical amplitude streaking and complex short-period multiples; however, the overall section looks more balanced in amplitude and does not exhibit strong first-order free-surface multiples.

Figure 5 presents an expanded 70 km near-offset section for the synthetic WAMo data. We note that Figure 4a would fall between 20 km and 40 km in this panel. Again, we clearly see the first two orders of free-surface multiples; however, in the upper shelf between 40 km and 70 km in distance, we now observe the in-

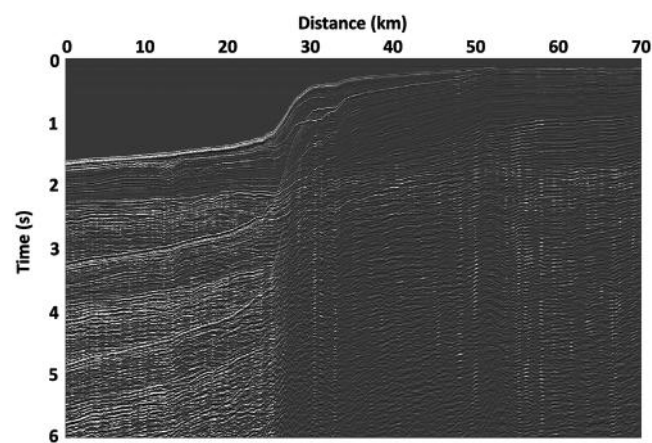


**Figure 5.** The 70 km inline section computed through the WAMo geomodel at the 32 km crossline coordinate. The up-shelf sections between 50 and 70 km show significant seismic imaging, inversion, and interpretation issues pertaining to reefs, short-period multiples, and internal multiples and scattering associated with the Bear Fm.

creasing complexity due to shallow carbonate reefs, strong variations in the shallow overburden, and the Bare Fm. The reef, located at 52 km, causes significant

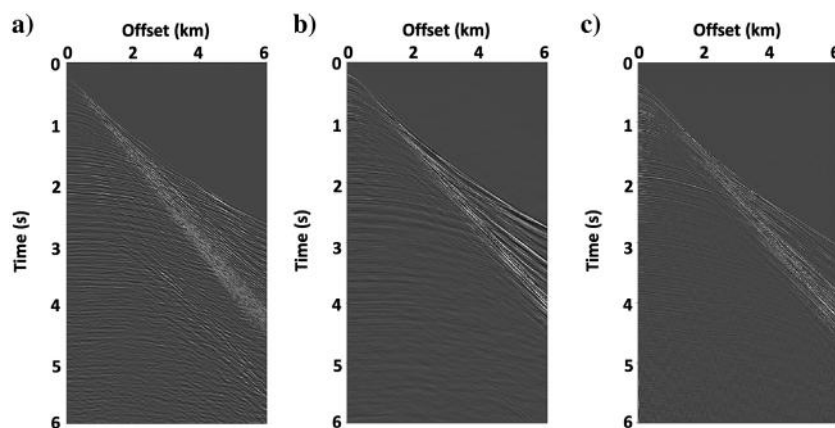
pull ups and additional wavefield complexity at all subsequent times. The hard and spatially variable water bottom between 57 km and 65 km in horizontal distance

causes significant lateral variations in the short-period free-surface multiples. The Bare Fm, visible at 1.0–1.3 s TWTT between 50 km and 70 km horizontal distance, demonstrably generates significant internal multiples and other full-wavefield scattering that causes strong amplitude (de)focusing and obscures the underlying reflectivity. Overall, these modeled seismic data are very representative of three important NCB imaging, inversion, and interpretation challenges.

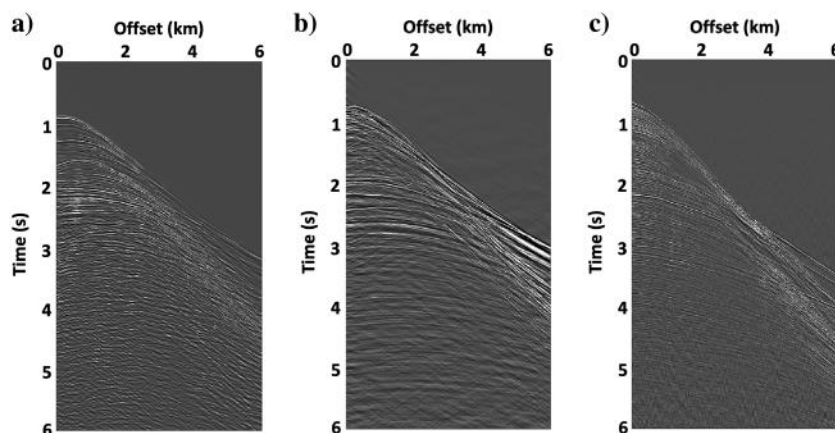
### Shot-gather comparison

Figure 6 presents a set of shot-gather comparisons between representative 2D WAMo synthetic data and 3D NCB marine seismic data for a shallow-water scenario. Figure 6a shows a 2D WAMo synthetic shot gather from the 32 km cross section sail line. Near offsets are dominated by short-wavelength reflectivity that includes several weak multiple contributions. Mid offsets exhibit a strong degree of “shingling” indicating the presence of shallow wave-guide behavior. Far offsets show a fully developed early arrival refracted component of the wavefield with fairly significant complexity. Refracted multiples are also evident at later times and farther offsets. Figure 6b shows a single cable from a 3D Wheatstone broadband shot gather. The character is fairly similar to the previous panel; however, the frequency content is more broadband and the early arrival far-offset refracted wavefield components now appear as more distinct arrivals. Weaker refracted multiples are also evident at mid to far offsets. Figure 6c shows an inline cable extracted from a 3D NCB conventional streamer shot gather. The data in this panel again show many of the same characteristics as the previous two panels. Differences include a somewhat higher frequency content, brighter near-offset reflectivity, and a less complex early arrival refracted wavefield component.

Figure 7 presents a second set of comparative shot gathers for a shelf-break location. Figure 7a shows the 2D WAMo synthetic shot gather, which exhibits more short-wavelength scattering behavior relative to Figure 6a, and a



**Figure 6.** Data comparison for the shelf location between (a) 2D modeled synthetic with (b) 3D Wheatstone broadband and (c) 3D NCB conventional seismic data sets.



**Figure 7.** Data comparison for the shelf break location between (a) 2D modeled synthetic with (b) 3D Wheatstone broadband and (c) 3D NCB conventional seismic data sets.

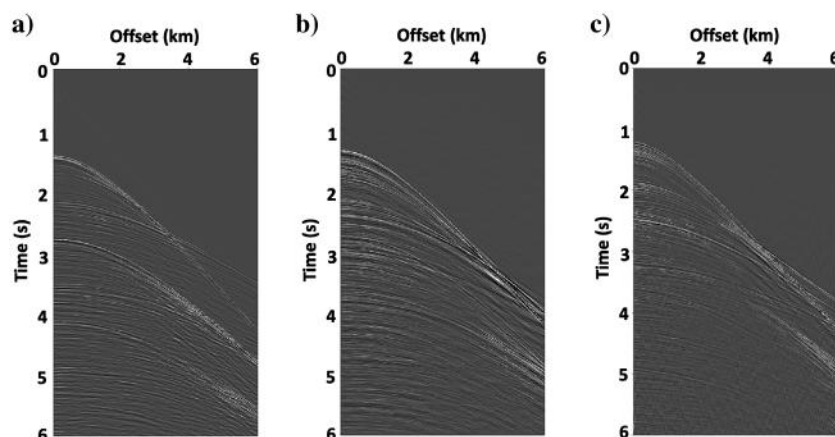


**Figure 8.** Data comparison for the deepwater location between (a) 2D modeled synthetic with (b) 3D Wheatstone broadband and (c) 3D NCB conventional seismic data sets.



significant increase in the number of hyperbola apices located at nonzero offsets. The refracted wavefield component is also dimmer than observed previously in Figure 6a. Figure 7b presents the 3D Wheatstone broadband shot gather, which shows more complex near-offset reflectivity as well as a more fully developed, far-offset, early arrival refractions. An increase in scattering is evident throughout the full panel relative to Figure 6b. Figure 7c presents the 3D NCB conventional shot gather, acquired in somewhat shallower water and a more benign shelf-break than that observed in Figure 6a. Relative to the WAMo synthetic data, the near offsets again show brighter short-wavelength reflectivity, whereas the mid to far offsets show more fully developed early arrival refracted wavefield components — though strikingly different than those in Figure 6b.

Figure 8 presents a third set of comparative shot gathers for a deepwater setting. Figure 8a shows the 2D WAMo synthetic results, in which the first- and

second-order multiples are now clear, and increased brightening is observed at mid-to-far offsets. Figure 8b presents a 3D Wheatstone broadband shot gather, which shows fairly bright near-offset reflectivity, a clear first-order multiple arrival, and similar brightening at mid to far offsets. Figure 8c presents the 3D NCB conventional shot gather, which contains bright near offsets, a weak first-order multiple arrival, and again brightening at mid to far offsets.

Overall, the seismic modeling results in Figures 6–8 demonstrate that the synthetic and field data sets generally have similar characteristics and also show not insignificant variations between them. However, differences between the two field data sets arguably exist to similar degree as between the synthetic and field data sets. Overall, we note that it would be challenging to correctly identify which panels are synthetic and which are from real marine streamer data, thus demonstrating the quality of our 3D geomodeling seismic modeling approaches.

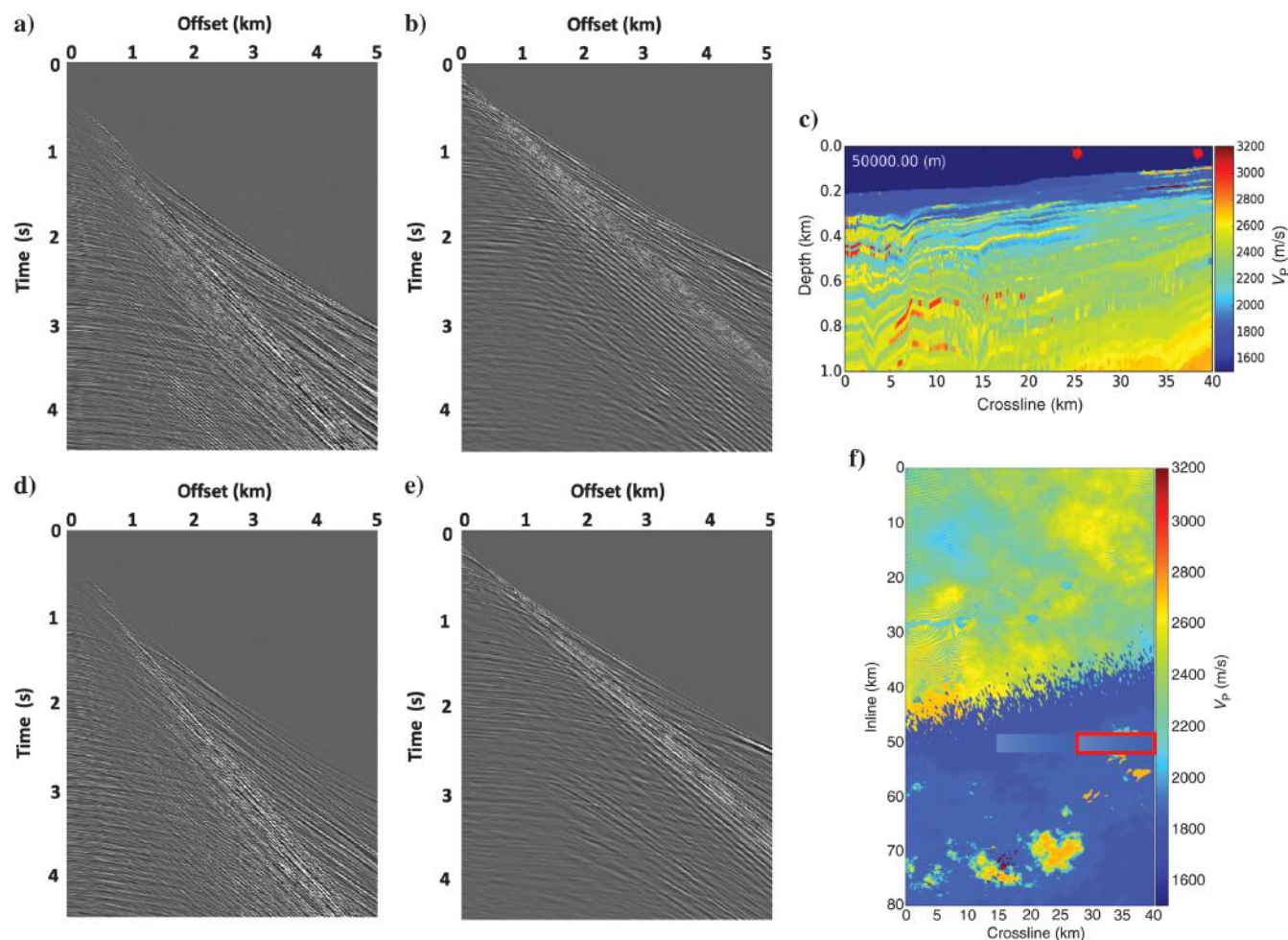


**Figure 9.** Comparison of field and synthetic shot gathers in shallow water on and off of a reef complex. (a) Woodside and (b) WAMo 3D shot gathers over reef complex. (d) Field data and (e) WAMo 3D shot gathers off of reef close to shots in (a and b). (c) Depth section showing the location of the shot gathers in (b and e) as right and left red star. (f) Map view showing the modeling aperture of the 3D shot gather. The red rectangle corresponds to (b), whereas the gray area without a red highlight is (e).

## Modeling around reef geobodies

One of the interesting capabilities of having a realistic and well-calibrated geomodel is that one can undertake modeling studies that aim to recreate observed complex full-wavefield phenomena. Figure 9 highlights one such study around a near-surface reef complex modeled as geobodies. Figure 9a presents a field-data shot record from a Woodside 2D data set that was acquired in shallow water over a reef complex. The near offsets are strongly contaminated with short-period multiples, almost to the point at which they obscure deeper reflections. The mid-to-far offsets are strongly dominated by refracted multiples that arrive for almost 2.5 s after the first refraction. Figure 9b presents the center sail line extracted from a 3D WAMo synthetic shot gather modeled over the shallow reef complex shown at the location shown by the right-hand star in Figure 9c (Figure 9f shows a map view of the simulated acquisition footprint, denoted by the red rectangle). The synthetic shot gather exhibits similarly strong multiply refracted mid-to-far offset arrivals that largely obscure the underlying reflections. The complexity of this arrival should be expected considering the near-surface complexity of the  $V_P$  model in Figure 9c to the left of the right red star. Figure 9d shows a field shot gather acquired along the sail line, but away from any known shallow reef structures. Comparing Figure 9a and 9d, it is evident that the multiple refracted arrivals have weakened. This effect is noted in the synthetic shot gather shown in Figure 9e (see Figure 9b), which was computed at the location of the left red star in Figure 9c and with the gray rectangle in Figure 9f to the left of the red rectangle.

Figure 10 presents another further modeling example extracted from a 3D shot record acquired over a very shallow reef (50 m minimum depth). The red rectangle on the inset map shows the acquisition geometry with the shot location being located midway north-south and 3 km from the eastern end of the model. The shot gather exhibits much of the same character as observed in Figure 9; however, there is a significant

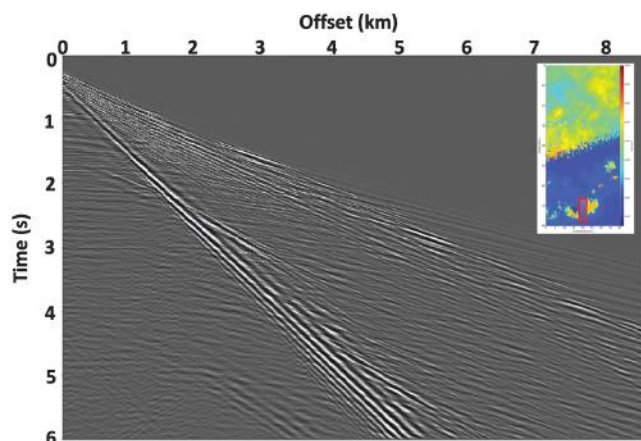


**Figure 10.** Example of a Scholte wave generated through wavefield interaction with a complex near-surface carbonate platform.

slow arrival, which is a dispersive Scholte wave that arises from scattering from seafloor topographic features with significant contrast in elastic properties (Zheng et al., 2013). This strong arrival also gives rise to additional refracted waves that arrive in advance of the main Scholte wave packet. Overall, these examples illustrate the capability of the geomodel to reproduce field data observations in complex geologic scenarios.

## 2D imaging tests

We undertook a series of 2D migration tests to investigate the image quality resulting from the 2D WAMo data simulations. Figure 11 shows a comparison between an RTM of the 2D WAMo synthetic data set (Figure 11a) and a representative PSTM result extracted from the 3D field seismic mega-merge volume (Figure 11b). Note that the field-data section was selected to roughly match the shelf-break geometry, and no multiple suppression was applied in either case (see below shelf break). Overall, the character of the two images is broadly consistent, with the main chronostratigraphic surfaces well-imaged (where present). However, the 3D mega-merge section exhibits somewhat greater reflector continuity, increased amounts of shorter wavelength reflectivity sequences in the zone 0.5–1.0 km below the mudline, and a higher degree of deep-seated faulting (these deep fault structures were not included in the WAMo model).

Figure 12 presents three magnified sections from the 2D RTM image along with zero-offset  $V_P$  pseudologs com-

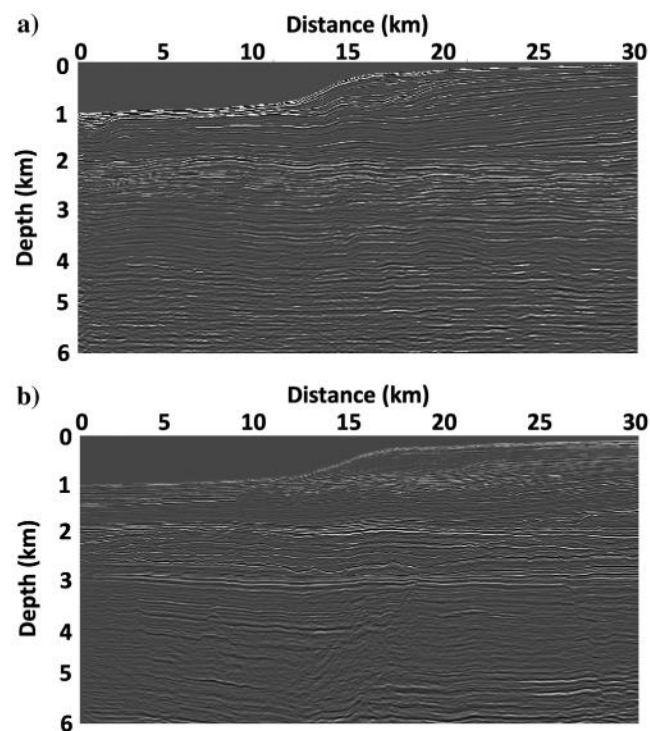


**Figure 11.** Comparison between (a) synthetic 2D RTM image at 32.0 km crossline and (b) PSTM image selected to match shelf-break geometry of (a) extracted from 3D field seismic mega-merge volume stretched to depth with the regional 3D migration velocity model.



puted from the WAMo model elastic parameters. The deepwater pseudolog (Figure 12a), along with the shelf-break (Figure 12b) and shallow-water (Figure 12c) counterparts, all show strong correlations between the RTM image amplitudes and the expected pseudolog values.

## Discussion

One of the most challenging aspects of the WAMo geomodeling procedure was calibrating the physical properties in the top 0.5–1.0 km below mudline. On the one hand, introducing strong short-wavelength variations in material properties significantly increased the scattering visible in modeled shot gathers and introduced wave-guide behavior such that little to no early arrival refracted energy was present. On the other hand, weakening near-surface heterogeneity nearly eliminated all scattering and wave-guide behavior and allowed for very clear refracted early arrivals, which

led to unrealistically dim or absent reflectivity. Finding a well-calibrated trade-off between these two end members proved to be a challenging task.

There were (at least) three key contributing factors giving rise to the difficulties in constraining the near-surface model: (1) a limited availability of wells logged within the top 500 m below mudline interval (due to limited economic incentive), (2) where wells logs were present, the data commonly indicated strong spatial heterogeneity and variability of material properties, and (3) the strong nonlinear dependence of seismic modeling on the near-surface model, in which even small changes to the underlying material properties could lead to significant changes within modeled shot-gather data.

Accordingly, the project team put significant emphasis on calibrating the near-surface viscoelastic model with an emphasis on wanting the overall character of simulated seismic data to match field data

while ensuring that the resulting material properties remained geologically and geophysically realistic. Finding this balance required undertaking a variety of “linear iterations” involving conditioning the existing 3D WAMo geomodel (e.g., applying 2D/3D smoothing and scaling operators), as well as multiple “nonlinear iterations” requiring remodeling the near-surface petrophysical relationships based on newly available geoscience information (e.g., geotechnical reports, International Ocean Discovery Program (IODP) drilling data) as well as analog data on geobody material properties from other similar geologic environments.

To illustrate the sensitivity of the WAMo model to near-surface variations,

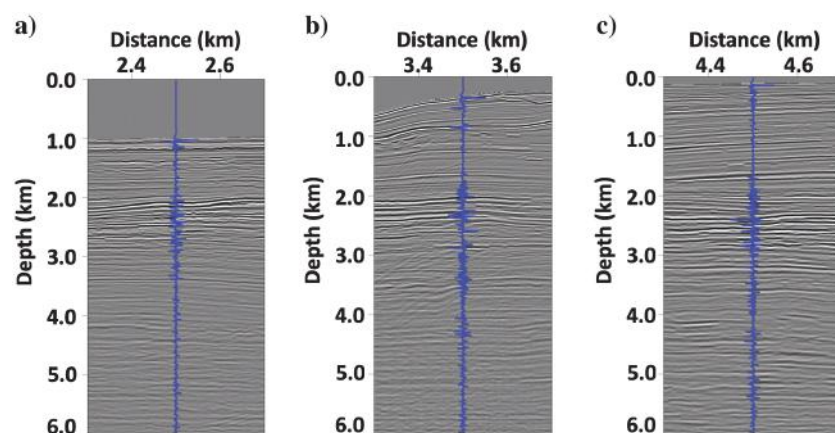


**Figure 12.** Overlay of RTM image at 32.0 km crossline distance with zero-offset  $V_P$  pseudowell reflectivity profiles computed from the WAMo model elastic parameters. (a) Deep water, (b) shelf break, and (c) shallow water.

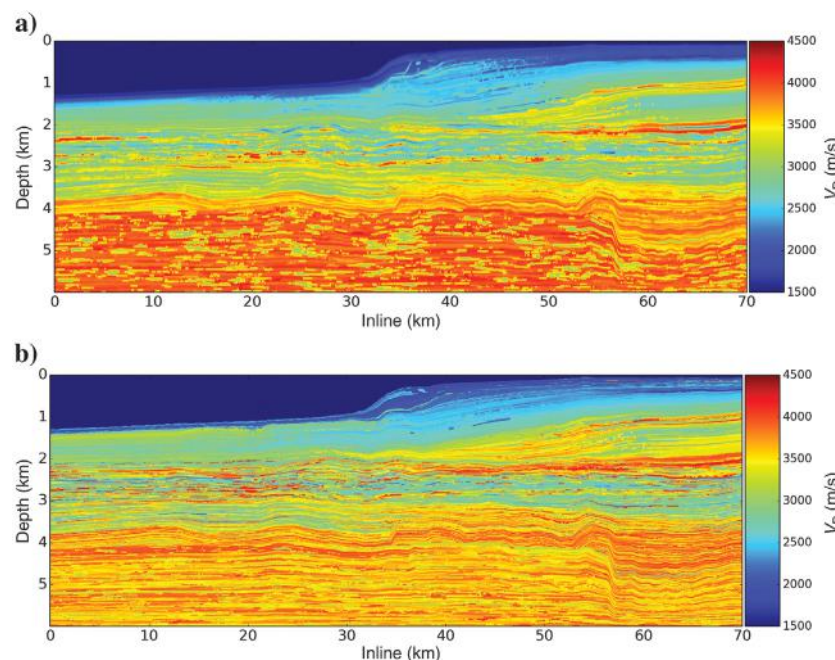


**Figure 13.** Earlier versions of the WAMo  $V_P$  model showing the range of model behavior. (a) Year 2 adjusted model with heavily smoothed top 0.5 km below mudline showing greatly reduced variation. (b) Year 3 original model with very strong vertical heterogeneity and updated deeper stratigraphy.

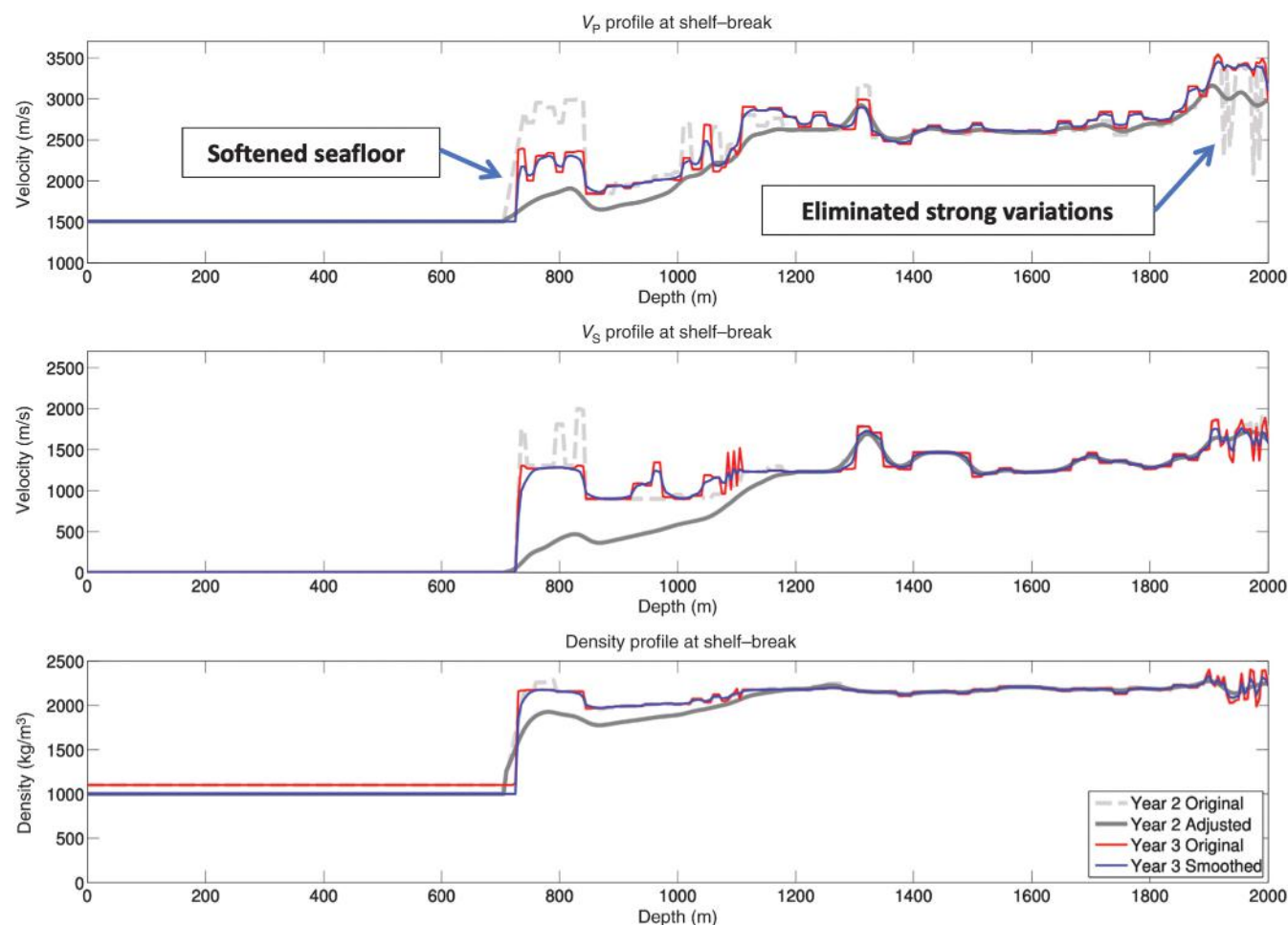


Figure 13 presents two earlier iterations of the WAMO model. Figure 13a shows the “year 2 adjusted,” which involved applying a strong taper to the “year 2 original” material properties at the water bottom that was linearly relaxed to 500 m below mudline. Figure 14 illustrates the results of applying the taper to the  $[V_P, V_S, \rho]$  material properties at a shelf-break model location along the 32 km crossline. The original elastic parameters for the top 2 km of year 2 original model, shown as a dashed gray line, show a very strong jump in material properties at the seafloor, followed by a low-velocity waveguide that introduced a strong series of multiply refracted wavefield arrivals. The results of applying the taper to the top 500 m to create the year 2 adjusted model are illustrated by the solid gray line, which shows that the material properties are now greatly smoothed with significantly diminished complexity. Figure 15a shows the corresponding nearest-offset section computed for the year 2 adjusted model. In comparison with Figure 4a, this section appears to be significantly lower frequency with unrealistically weak reflectivity between 1.0 s and 1.5 s after the imaged seafloor reflector.

Figure 13b shows the “year 3 original” model, which required a nonlinear iteration of the petrophysical

modeling relationship that reintroduced short-wavelength heterogeneity into the WAMO model material properties. The red lines in Figure 14 show the result of applying the nonlinear petrophysical update to generate the year 3 original model (Figure 13b). This update restored some of the vertical heterogeneity present in the year 2 original model, including some fairly short-wavelength strong-contrast stratigraphic variations. Figure 15b presents the corresponding nearest-offset section for the year 3 original model. The data clearly are much higher frequency and show more short-wavelength reflectivity than in Figure 15a; however, the heterogeneity effects are now too strong and the third (and perhaps the fourth)-order multiples are now visible in the deepwater and shelf break regions.

Addressing these model deficiencies required an additional linear iteration involving the above model smoothing procedure to remove approximately 50% of the strong model heterogeneity. The blue lines in Figure 14 show the final year 3 smoothed model (Figure 3b) after applying the final model smoothing procedures. The nearest-offset section of the final WAMO model (Figure 4a) now has a weaker level of scattering,



**Figure 14.** Pseudolog examples at the up-shelf location showing the differences among the year 2 original model, year 2 adjusted model, year 3 original model, and the “Y3 smoothed” model used for the 2D/3D viscoelastic simulations.

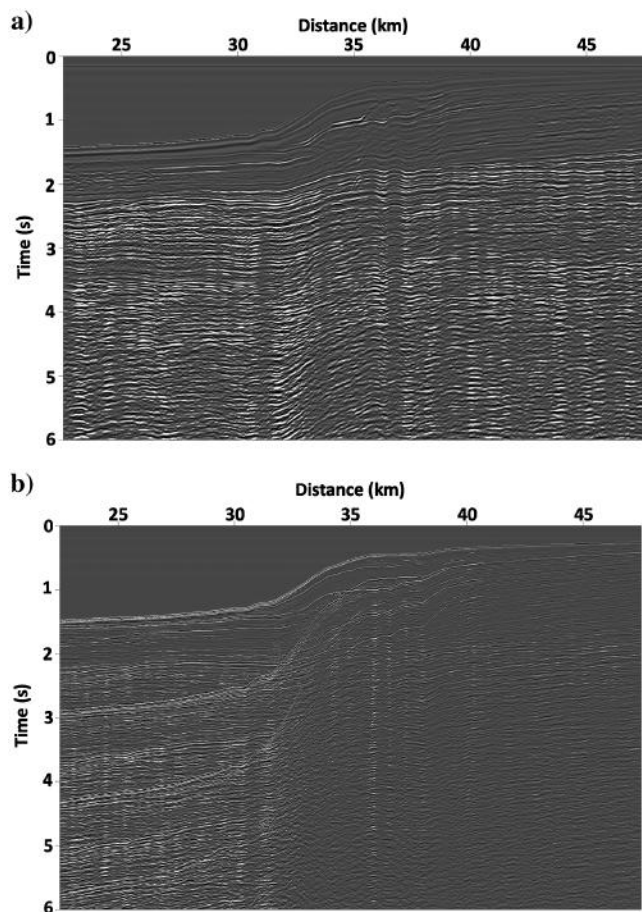


**Figure 15.** Earlier versions of the WAMo  $V_p$  model showing the range of model behavior. (a) Year 2 adjusted model with heavily smoothed top 0.5 km below the mudline showing greatly reduced variation. (b) Year 3 original model with very strong vertical heterogeneity and updated deeper stratigraphy.

wave-guide effects, and has only very weak third-order multiples. Thus, it is becoming more consistent with the observed character of NWS seismic data.

Overall, this progression of examples shows that, in the absence of hard data constraints, it is difficult to avoid some model conditioning. However, with the help of seismic forward modeling, one may consider the match with field seismic data as “soft constraints” that can significantly help to define a geologically reasonable viscoelastic model.

## Conclusion

This paper presents the WA Model project and demonstrates that our geomodeling and seismic modeling methods can be used to develop and validate large-scale, realistic 3D earth models constrained by geologic, geophysical, and field seismic data. Starting from initial viscoelastic model parameters, we discuss in detail the fine tuning applied to calibrate the WAMo model so that it matches marine seismic shot gather and migrated image data. We discuss how we applied FD seismic modeling to simulate 2D/3D shot gathers with

common streamer acquisition geometry containing realistic frequency content and full-wavefield phenomena (i.e., reflectivity and scattering). The resulting 2D/3D near-offset sections and shot gathers share similar characteristics with those from two comparison marine seismic data sets. In particular, in regions containing near-surface reef geobodies, the synthetic shot gathers were able to recreate complex wavefield behavior (e.g., early arrival diving waves, wave-guide multiply refracted arrivals, and Scholte waves) commonly observed in WAs NWS. The resulting 2D images and pseudowells are similarly well-matched to field data observations, which help provide seismic “validation” of our 3D WAMo geomodel.

We also discuss the importance, and the challenges, of updating near-surface viscoelastic material properties, and the need for performing linear iterations involving numerical model conditioning as well as nonlinear iterations requiring full-model updating of the underlying petrophysical relationships. Because shallow petrophysical data are not commonly acquired in exploration wells, the nonlinear updates involved incorporating additional information (i.e., geotechnical data, results from analog geobody studies) as well as using soft constraints to match the overall character of NWS field seismic data. The final WAMo geomodel has been well-calibrated and demonstrated to match marine seismic data in the project area. Thus, it can be used for geophysical and geologic studies ranging from scenario testing of modular components through seismic FD modeling to examine novel imaging, inversion, and interpretation methods.

## Acknowledgments

The WAMo project was made possible by industry research consortium financial support of Apache/Quadrant, BHP Billiton, Chevron, DownUnder Geosolutions (DUG), Santos, Shell, and Woodside Ltd. The UWA WAMo project team would like to thank the following people for their comments and suggestions throughout the WAMo project: P. Chia, G. Duncan, A. Goldberg, G. Hampson, L. Hansen, F. Mancini, S. Lang, T. Payenberg, D. Sibley, O. Sundsby, T. Thomson, C. Walton, and G. Ward. The 3D WAMo mega-merge volume was kindly provided by L. Hansen (Apache/Quadrant). The regional time-to-depth velocity model was provided by DUG. We also thank Eliis, IHS, Kingdom, and Schlumberger for software grants that enabled much of the interpretation and data analysis work. We acknowledge the WA Petroleum Information Management System and the National Offshore Petroleum Information Management System for making geophysical and geologic data sets publicly available. Wavefield simulations were conducted using research HPC time grants from the Pawsey Center computational facilities (Kensington, WA, Australia).

## Data and materials availability

Nonconfidential data associated with this research are available and can be obtained by contacting the corresponding author.

## References

- Aki, K., and P. Richards, 1980, *Quantitative seismology: Theory and methods*: Freeman.
- Billette, F., and S. Brandsberg-Dahl, 2005, The 2004 BP velocity benchmark: 67th Annual International Conference and Exhibition, EAGE, Extended Abstracts, B035.
- Bohlen, T., 2002, Parallel 3-D viscoelastic finite-difference seismic modelling: *Computers and Geosciences*, **28**, 887–899, doi: [10.1016/S0098-3004\(02\)00006-7](https://doi.org/10.1016/S0098-3004(02)00006-7).
- Claerbout, J., 1998, *Geophysical estimation by example: Environmental soundings image enhancement*: Stanford University.
- Courant, R., K. Friedrichs, and H. Lewy, 1928, Über die partiellen differenzengleichungen der mathematischen physik: *Mathematische Annalen*, **100**, 32–74, doi: [10.1007/BF01448839](https://doi.org/10.1007/BF01448839).
- Doyen, P., 2007, Seismic reservoir characterization: An earth modelling perspective (EET 2): EAGE.
- Fehler, M., and P. Keliher, 2011, SEAM phase I: Challenges of subsalt imaging in tertiary basins, with emphasis on deepwater Gulf of Mexico: SEG.
- Gray, S., and K. Marfurt, 1995, Migration from topography: Improving the near-surface image: *Canadian Journal of Exploration Geophysics*, **31**, 18–24.
- Lee, J., and T. Mukerji, 2012, The Stanford VI-E reservoir: A synthetic data set for joint seismic-EM time-lapse monitoring algorithms: 25th Annual Report, Stanford Center for Reservoir Forecasting, Stanford University.
- Regone, C., J. Stefani, P. Wang, C. Gerea, G. Gonzalez, and M. Oristaglio, 2017, Geologic model building in SEAM phase II — Land seismic challenges: The Leading Edge, **36**, 738–749, doi: [10.1190/tle36090738.1](https://doi.org/10.1190/tle36090738.1).
- Shragge, J., J. Bourget, D. Lumley, T. Wilson, J. Giraud, A. Iqbal, M. Niri, B. Whitney, T. Potter, T. Miyoshi, and B. Witten, 2019, The Western Australia Modeling (WAMo) project — Part 1: Geomodeling: Interpretation, **7**, this issue, doi: [10.1190/int-2018-0217.1](https://doi.org/10.1190/int-2018-0217.1).
- Versteeg, R., 1994, The Marmousi experience: Velocity model determination on a synthetic complex data set: The Leading Edge, **13**, 927–936, doi: [10.1190/1.1437051](https://doi.org/10.1190/1.1437051).
- Zheng, Y., X. Fang, J. Liu, and M. C. Fehler, 2013, Scholte waves generated by seafloor topography: arXiv preprint, arXiv:1306.4383.



**Jeffrey Shragge** received a B.Sc.H. in physics from Queen's University, an M.Sc. in geophysics from the University of British Columbia, and a Ph.D. in geophysics from the Stanford Exploration Project at Stanford University. He is an associate professor in the Geophysics Department at the Colorado School of Mines and a coleader at the Center for Wave Phenomena research consortium. He was formerly the Woodside professor in computational geoscience and an associate professor jointly appointed in the School of Earth and Environment and

School of Physics at the University of Western Australia. His research interests include 3D wave propagation, 3D/4D seismic imaging and velocity inversion, near-surface geophysics, and scientific HPC.



**Toby Potter** trained as a computational astrophysicist and is the founder of Pelagos Consulting and Education. He has a keen interest in using computers to solve problems and showing others how to do the same. He was formerly employed as a postdoctoral researcher in geophysics at the Centre for Energy Geoscience at the University of Western Australia and now uses his experience to help companies and organizations bridge the gap between domain-specific knowledge and software craftsmanship. He is also a passionate science communicator and regularly engages with industry and academia in consulting and education roles.

**Jérémié Giraud** received a B.S. and an M.S. Eng in applied geophysics from the School and Observatory of Earth Sciences, University of Strasbourg (Strasbourg, France). He received his Ph.D. (2018) from the Centre of Exploration Targeting (CET), University of Western Australia (Perth, Australia). He is currently a research fellow at the CET as part of the Loop and MinEx CRC consortia. His research interests include the development of geophysical inversion techniques focusing on the interaction between geophysics, geology, and petrophysics.



**Mohammad Emami Niri** received a B.S. and an M.S. in petroleum exploration engineering. He received a Ph.D. in geophysics from the University of Western Australia. He has been an assistant professor at the Institute of Petroleum Engineering of the University of Tehran since 2015. After completing his B.S. and M.S. degrees, he worked for oil and gas companies as a geophysicist for more than six years. His current research and applied industry work interests include seismic reservoir characterization, rock physics, geostatistical reservoir modeling, and machine learning in reservoir modeling/simulation.



**Beau Whitney** is a quaternary geologist and paleoseismologist who specializes in seismic source characterization to use in seismic hazard assessments. Stable continental regions (SCRs) are uniquely complex for seismotectonic characterization due to limited seismological data and a lack of known active earthquake fault sources, yet they encompass most of the earth's surface, are inhab-



ited by billions of people, and house numerous critically sensitive infrastructure such as nuclear facilities. He has innovated strategies for developing seismotectonic models and characterizing earthquake occurrence behavior in intraplate regions to improve upon the typical state of practice currently used in seismic hazard analysis for these parts of the globe. He provides expertise in the framework of the Senior Seismic Hazard Assessment Committee for nuclear power plants and storage facilities. These critical infrastructures have engineering design tolerances that are often

controlled by low-frequency, moderate-magnitude events that dominate the seismic hazard in intraplate settings. His research focus and specialization is in intraplate regions where low slip rates and infrequent earthquake occurrence (or SCRs) limit the data available for statistically robust seismic hazard analysis.

Biographies and photographs of the other authors are not available.